COMMUNICATION

Efficient Lithium-Ion Storage Using Heterostructured Porous Carbon Framework and Its in situ Transmission Electron Microscopy Study

Received 00th January 20xx,
Accepted 00th January 20xx

DOI: 10.1039/x0xx00000x

Minjun Kim,[+a] Joseph F.S. Fernando,[+b] Jie Wang,*[c] Ashok Kumar Nanjundan,*[a] Jongbeom Na,[a] Md. Shahriar A. Hossain,[a] Hiroki Nara,[c] Darren Martin,[d] Yoshiyuki Sugahara,[c,e] Dmitri Golberg*[b] and Yusuke Yamauchi*[a,c,f]

Heterostructured porous carbon framework (PCF) composed of reduced graphene oxide (rGO) nanosheets and MOF-derived microporous amorphous carbon is prepared to investigate its potential use in a lithium-ion battery. As an anode material, PCF exhibits efficient lithium-ion storage performance with high reversible specific capacity (771 mA h g^{-1} at 50 mA g^{-1}), excellent rate capability (448 mA h g^{-1} at 1000 mA g^{-1}), and long lifespan (75 % retention after 400 cycles). *In situ* transmission electron microscopy (TEM) study demonstrates that its unique three-dimensional (3D) heterostructure can largely tolerate the volume expansion. We envisage that this work may offer deeper understanding of the importance of tailored design of anode materials for future lithium-ion batteries.

With the evolving global awareness on carbon emissions and climate changes caused by the consumption of fossil fuels, there has been a significant effort to shift the global energy markets towards the renewable energy sources. As both quality and quantity of renewable energies dramatically improve, lithium-ion batteries (LIBs) have gained an enormous attention as one of major means to store the excess renewable energy for the later usage. Typically, LIBs exhibit unique advantages such as high energy density, wide operating voltages, and highly reversible charge-discharge processes. They are therefore more practical and applicable to the advancing smart technologies and electrical vehicles as compared to other energy storage devices.[1] In the commercial LIBs, graphite is commonly adopted as anode material due to its high electrical conductivity, physical and chemical stabilities, and cost-effectiveness. Poor rate capability and low theoretical capacity (372 mAh g^{-1}) of graphite, however, stand as major bottlenecks in achieving higher power/energy densities in LIBs. This consequently leads to an increasing research interest for alternative anode materials that satisfy both large current discharge capacity and high reversible capacity requirements.[2, 3]

Carbon anode materials (*e.g.*, carbon nanofibers,[4] carbon nanotubes (CNTs),[5] porous carbon,[6] and rGO[7]) offer promising electrochemical performances in LIBs, because of their good cyclability and charge-discharge kinetics. Porous carbon materials, especially, hold a significant potential in LIBs. Typically, their interconnected open pores can efficiently reduce the diffusion distance of Li ions and tolerate the volume expansion, thus alleviating capacity fading of the materials.[8, 9] The fabrication processes of porous carbon materials however are often complicated and expensive, thus largely limiting scale-up manufacturing process and commercialization.[10, 11] Besides, monomodal pore system can be unsuitable as electrode material for batteries. To achieve suitable pore sizes, hierarchical porous structures are highly desirable because they encompass the advantages of pores of different diameters.[12] Apart from the structural hurdles, a challenge remains in achieving optimal surface functionalization of porous carbon to further improve the reversible capacity of the materials.[13, 14]

Graphene is a two-dimensional network of carbon atoms bonded together *via* sp^2 hybridization, and it has received an enormous research attention because of its high specific surface area (SSA), outstanding physical and chemical stabilities, and electrical conductivity.[15-17] Consequently, as the anode material, graphene offers high reversible capacity at relatively low current densities through the formation of Li_2C_6.[18] However, it undergoes serious restacking and aggregation at high current densities, thus hindering efficient insertion/extraction of Li ions.[19, 20] Alternatively, assembling graphene into a 3D porous nanostructure helps to separate graphene layers, hence largely preventing their restacking.[21] A 3D porous nanostructure of graphene generally demonstrates improvement in rate capability and cyclability as it allows efficient transfer of Li ions to highly accessible active

a *Australian Institute for Bioengineering and Nanotechnology (AIBN) and School of Chemical Engineering, The University of Queensland, Brisbane, Queensland 4072, Australia.*
b *Centre for Materials Science and School of Chemistry and Physics, Queensland University of Technology (QUT), 2 George Street, Brisbane, Queensland, 4000, Australia*
c *JST-ERATO Yamauchi Materials Space-Tectonics Project, Kagami Memorial Research Institute for Science and Technology, Waseda University, 2-8-26 Nishi-Waseda, Shinjuku, Tokyo 169-0051, Japan*
d *JST-ERATO Yamauchi Materials Space-Tectonics Project and International Center for Materials Nanoarchitechtonics (WPI-MANA), National Institute for Materials Science (NIMS), 1-1 Namiki, Tsukuba, Ibaraki 305-0044, Japan*
e *Department of Applied Chemistry, School of Advanced Science and Engineering, Waseda University, 3-4-1 Okubo, Shinjuku-ku, Tokyo 169-8555, Japan*
† *These authors equally contributed to this work.*

components. For instance, integrating scaffold materials, such as porous carbon spheres, with graphene can effectively buffer the volume expansion, and promote the diffusion of electrolytes into its interconnected carbon network.[22] However, it is still challenging to achieve a homogeneous distribution of the scaffold materials between graphene layers.[23]

In this study, we investigate the high potential of our previously reported 3D porous carbon framework (PCF) prepared from the hybrid materials consisting of GO and metal–organic frameworks (MOFs) as the anode material for LIB.[24] A type of MOF, known as zeolitic imidazolate framework-8 (ZIF-8), is highly microporous material enriched with carbon (C) and nitrogen (N) atoms. Based on our recent method, we successfully hybridized oppositely charged GO and ZIF-8 (~225 nm in diameter) *via* electrostatic assembling, followed by vacuum filtering to finally obtain a ZIF-8/GO hybrid structure (**Fig. S1**).[24] Direct pyrolysis results in PCF with a continuous heterostructure having microporous carbon layer coated by the rGO surface (**Fig. S2**). As-synthesized PCF demonstrates the following advantages as the anode material in LIB: (1) Use of ZIF-8 as a carbon precursor and template allows to form uniform hollow carbon polyhedron with tuneable cavity dimensions; (2) Abundant N atoms in ZIF-8 ensure the uniform heteroatom doping of PCF, thus contributing to an increase in Faradaic reactions with Li ions; (3) Homogeneous 3D structures of PCF demonstrate the orderly stacked graphene-like structures which lead to good cyclability and rate capability; (4) Hierarchical porosity of PCF allows suitable pore sizes and surface areas to significantly reduce the ion diffusion distance, thus promoting the Li ion insertion/extraction for stable electrochemical kinetics. The main target of the current work is to demonstrate efficient Li-ion storage using our PCF and to investigate charge/discharge behaviour of Li ions through an advanced *in situ* transmission electron microscopy (TEM).

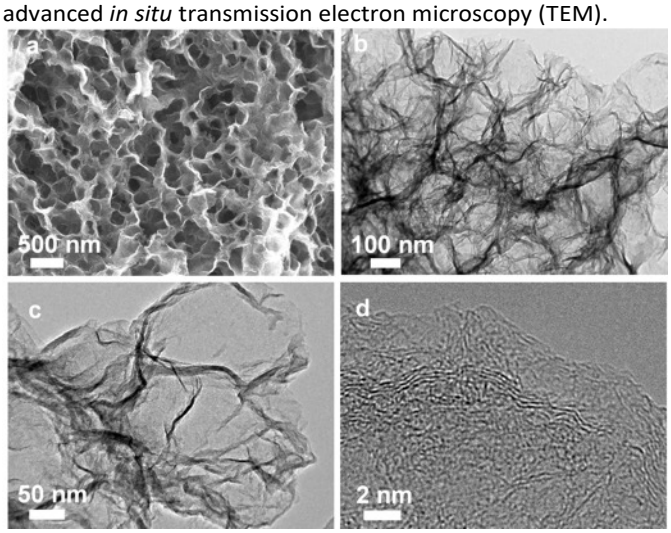

Fig. 1 a) Scanning electron microscopy (SEM), b-c) TEM, and d) HRTEM images of PCF.

From the scanning electron microscope (SEM) image, it is clearly seen that the ZIF-8 particles are uniformly wrapped by GO nanosheets (**Fig. S3**). Typically, PCF consists of the interconnected rGO nanosheets and well-dispersed hollow cavities (~200 nm in diameter) (**Fig. 1a**). The transmission electron microscopy (TEM) image further confirms that the hollow cavities are polyhedron-shaped and are physically interfaced with the surrounding layers of rGO (**Fig. 1b, c**). Furthermore, the high-resolution TEM (HRTEM) image (**Fig. 1d**) clearly indicates that PCF exists as the heterostructured carbon network consisting of ZIF-8 derived amorphous carbon and graphitized carbon layers of rGO. PCF demonstrates increased level of graphitization and substantial level of pyridinic and graphitic nitrogen species, as well as high SSA (643 m^2 g^{-1}) and pore volume (0.35 cm^3 g^{-1}), which are highly desirable as LIB anode material. More detailed discussion on the characterization can be found in Supporting information (**Fig. S4-S6, Table S1**). The overall electrochemical performance of PCF as anode material was then thoroughly investigated.

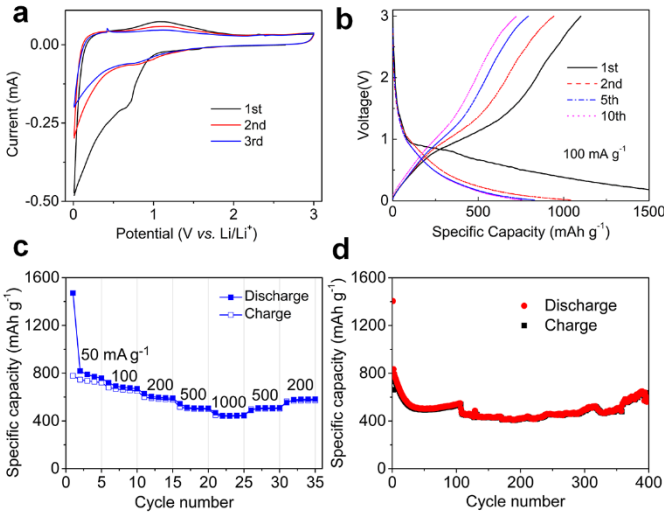

Fig. 2 Electrochemical performance of PCF as anode electrode in LIB. (a) CV curves at 0.2 mV s^{-1}. (b) GCD curves at 100 mA g^{-1}. (c) Rate capability at a range of current rates (50 to 1000 mA g^{-1}). (d) Long-term cycling performance at a current density of 100 mA g^{-1}.

Fig. 2 represents the electrochemical performances of PCF anode measured in a voltage range of 0.01-3.0 V, which is commonly adopted to test half-cells consisting of Li metal and carbon materials.[18-20] The first cyclic voltammetry (CV) curve measured at 0.2 mV s^{-1} demonstrates a strong cathodic peak at ~0.64 V which is mainly generated by the irreversible formation of solid electrolyte interphase (SEI) layer (**Fig. 2a**).[2] In addition, a distinct voltage hysteresis is observed during the delithiation process in the CV curves, indicating the removal of inserted Li ions from 0.01 to 3.0 V. Typically, extraction of Li ions from the graphite layers takes place at 0.16 V, and Li ion desorption occurs at around 1.0 to 1.5 V.[30, 31] Capacity between 2.0 and 3.0 V is dominantly derived from double layer capacitance of PCF surface, however, the Faradaic reaction of heteroatoms on the surface of PCF slightly contributes to the capacity, as confirmed by the CV curves as a weak anodic peak.[30] The CV curves of the following cycles are largely overlapping with each other, thus indicating highly reversible capacity of PCF electrode (**Fig. 2a**).

The first capacities of discharge and charge of PCF electrode can reach as high as 1536 and 678 mAh g^{-1} at 500 mA g^{-1}, respectively, resulting in a low Coulombic efficiency of 44 % (**Fig. 2b**). Such low Coulombic efficiency of the first cycle is largely due to potential side reactions leading to the formation of SEI composed of LiF, LiOH, Li_2O, Li_2CO_3 and organic compounds such as lithium alkyl carbonate in the cell.[32,33] It is possible to have Li ions being trapped in the voids or pores and/or chemically fixed at the vicinity of heteroatoms in an irreversible manner, thus leading to a capacity loss, and subsequent

fluctuations in the prolonged cycling performance.[34, 35] Highly stable and reversible charge-discharge capacity and much higher Coulombic efficiency are observed from the second cycle onwards (**Fig. 2b**). This observation can be directly correlated with the CV curves, in which the significant reduction current in the first cycle starts to fade in the subsequent cycles. A lithiation capacity of approximately 500 mAh g^{-1} in the 3rd cycle is observed, which is greater than the theoretical specific capacity of graphite (372 mAh g^{-1}) and previously reported anode materials (**Fig. 2b, Table S2**). Upon lithiation at a voltage greater than 0.5 V, Li ions adsorb onto the surface of PCF, intercalate into the carbon defects, and react with heteroatoms.[30, 36] The Li ion storage mechanism of PCF is therefore not limited to the intercalation, but also involves other mechanisms such as surface adsorption of Li ions and Faradaic process at heteroatom-doped sites, hence allowing PCF to demonstrate a high specific capacity.[34]

The rate tolerance of PCF anodes was examined by the discharge capacities obtained at various current densities from 50 to 1000 mA g^{-1} (**Fig. 2c**). Specific discharge capacities of 771, 604 and 448 mAh g^{-1} are observed at 50, 200 and 1000 mA g^{-1}, respectively. These discharge capacities are significantly higher than values of the previously reported carbon anode materials at the same current densities.[25, 31, 37] Furthermore, the ability of PCF electrode to recover its original capacity of ~ 604 mAh g^{-1} at 200 mA g^{-1} after cycling at higher current densities indicates its superior rate tolerance at various current densities (**Fig. 2c**). The cycling performance of PCF electrode was also investigated under 400 consecutive galvanostatic charge–discharge (GCD) cycles between 0.01 and 3.0 V at 100 mA g^{-1}. A certain level of capacity loss is observed in the first few cycles potentially due to the irreversible trapped Li ions and SEI formation (**Fig. 2d**).[37] Even after 400 GCD cycles, PCF electrode shows high-capacity retention. Notably, the specific capacity value (594 mAh g^{-1}) at the 300th cycle is about 75 % of the third discharge capacity (795 mAh g^{-1}) at 100 mA g^{-1}. After few initial cycles, the Coulombic efficiency of PCF reaches 99–100 %. Excellent rate capability, high reversible capacity and cyclability of PCF demonstrate its high potential as anode material for LIBs.

To study the structural stability and the reaction mechanism of PCF as anode, direct *in situ* TEM experiments were conducted. Specifically, PCF was attached to the gold electrode, while a piece of Li was put on the tungsten (W) counter-electrode whose fine movement was controlled by a piezo-motor to visualize structural and volume variations of PCF during lithiation/delithiation (**Fig. 3a**). To corroborate the repeatability of *in situ* TEM measurements two separate clusters of PCF sample were studied, cluster 1 (**Fig. 3b-d**) and cluster 2 (**Fig. 3e-h**). TEM image (**Fig. 3b**) shows PCF cluster 1 on the stationary Au electrode, and a layer of Li metal at the piezo-driven W probe of a scanning tunnelling *in situ* TEM (STM-TEM) holder. In the nano-battery setup, a layer of Li_2O was formed on the Li metal once the holder was first exposed to the air before its insertion into TEM column. This oxide layer served as a solid electrolyte in the nano-battery setup. The red arrow indicates the contact point of Li/Li_2O counter electrode on PCF cluster 1. **Fig. 3c** represents a magnified TEM image of PCF sample and the corresponding selected area electron diffraction (SAED) pattern before contacting with the counter electrode. The two rings observed on the SAED correspond to {101} and {112} planes of graphitic carbon. Once the sample was approached and touched with the piezo-driven Li/Li_2O electrode, a bias of -3.0 V *vs.* Li was applied to facilitate a lithiation of PCF because of overvoltage due to Li_2O solid electrolyte and limited contact area of PCF. **Movie S1** displays the recording of the lithiation process. The recording itself does not show obvious changes to the sample, however a careful comparison of TEM images and SAED patterns before and after lithiation give some insights. The width of cluster 1 was monitored across two points, as marked by a red arrow in **Fig. 3c-d**. The width increased from 737 nm to 744 nm denoting a negligible expansion of only ~ 1 % across this direction. In addition, the graphitic regions (edges

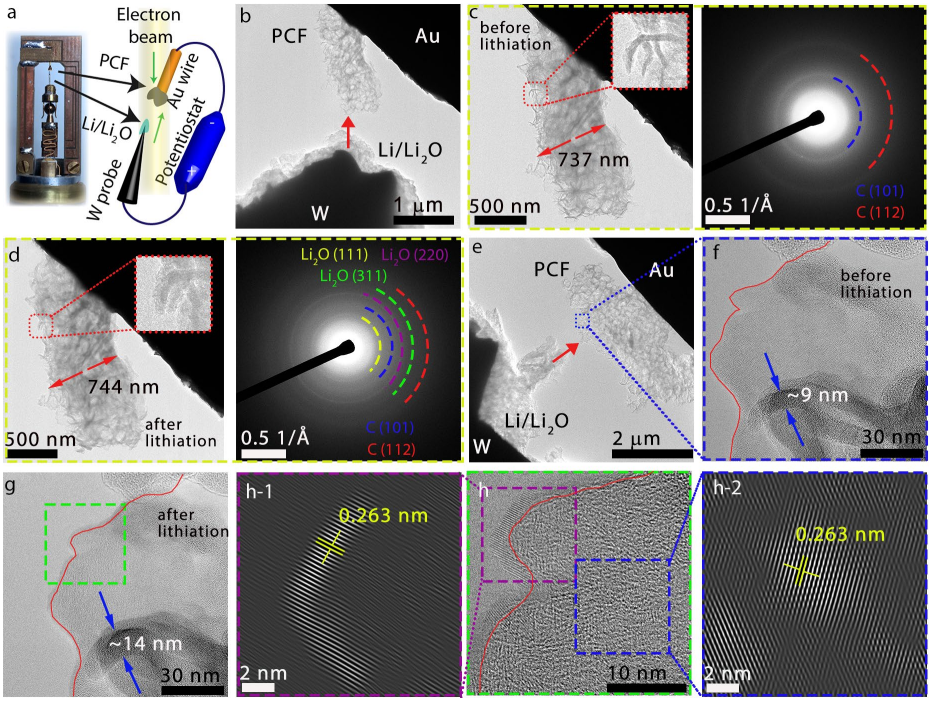

Fig. 3 (a) Schematic of the electrochemical cell assembled inside a high-resolution transmission electron microscope. (b) TEM image of the experimental cell setup before contacting the sample. (c) A zoomed-in TEM image and the SAED pattern of the PCF cluster 1 before lithiation. Inset of (c) shows a magnified view of the region marked in red. (d) TEM image and the SAED pattern of the same sample area after 1st lithiation (**Fig. S7** shows the area selected for electron diffraction). Inset in (d) shows a magnified view of the region marked in red. (e) TEM image of the experimental cell setup before the lithiation of the PCF cluster 2. (f) A zoomed-in image of the framed area in (e). (g) TEM image of the same sample area (PCF cluster 2) after the 1st lithiation. (h) High resolution TEM image of the framed region in (g). h-1 and h-2 display inverse FFT images of marked regions in (h).

of hollow cavities) show some expansion as indicated in the insets in **Fig. 3c** and **3d** (the expansion of graphitic region will be noted further when discussing PCF cluster 2 below). Interestingly, after lithiation, additional diffraction rings appeared in the SAED pattern, corresponding to {111}, {220} and {311} planes of crystalline Li_2O (**Fig. 3d**). The diffraction rings corresponding to graphitic carbon became less intense/broadened likely due to the insertion of Li^+, formation of Li_2O and a change in the interlayer spacing (Note: as shown in **Fig. S7**, SAED pattern was collected from a selected region in the centre of the sample after retracting the Li/Li_2O counter electrode). Moreover, SAED patterns were analysed by converting them to 1D profiles as shown in **Fig. S8**). To have a deeper understanding of the Li_2O formation within PCF material, high resolution TEM imaging was performed on a region of PCF cluster 2 (blue square marked in **Fig. 3e** and **3f**) before and after the lithiation process. The graphitic region (edge of cavity) shows an increase in width from 9 to 14 nm after lithiation (**Fig. 3g**), denoting an expansion of ~55 % probably due to Li_2O formation between the graphite interlayers. However, owing to the unique interconnected cavities of PCF material, the overall volume expansions remain remarkably low as discussed earlier. **Fig. 3h** shows the high resolution TEM image of the region marked in **Fig. 3g** (green square), while **Fig. 3h-1** and **3h-2** show inverse FFT images of marked regions in **Fig. 3h**. Intriguingly, there is a clear evidence for a crystalline substance formed along the border of PCF sample after lithiation (**Fig. 3h-1**). Careful analysis shows that crystallinity also develops within the material **(Fig. 3h-2)**. The measured interlayer spacing of 0.263 nm can be attributed to the (111) planes of Li_2O. Formation of Li_2O throughout PCF in fact indicates successful insertion of Li^+ ions. The presence of O-containing functional groups (**Fig. S5**) within PCF materials could have promoted the formation of Li_2O. A potential of +3 V *vs*. Li could be applied to trigger delithiation. Interestingly, much of the crystalline Li_2O disappeared from the material indicating structural reversibility (**Fig. S9**). Some Li_2O remained inside and along the border of the material, which also accounts for the low Coulombic efficiency in the first cycle. Li_2O is a major component in the SEI layers of graphite-based LiBs.[38] Although a real SEI cannot be formed in the nanobattery device (due to the absence of an organic electrolyte), the Li_2O outer layer is reminiscent of a stable SEI layer which is important to ensure long cycle life of the material. In summary, PCF material manifests an excellent structural stability and reversible Li (de)insertion capability owing to its unique structure comprising of interconnected rGO nanosheets and hollow cavities. In conclusion, due to the prominent 3D porous structure and surface chemical properties, our PCF demonstrates high reversible specific capacity, excellent rate capability as well as long lifespan as the anode material of LIBs. *In situ* TEM study accompanied with analysis of voltage/current profiles provides in-depth understanding of lithium insertion processes in PCF structures. This work therefore presents the direction of the future investigation and development of next-generation MOF-derived carbon materials for more advanced secondary battery applications.

This work was supported by the JST-ERATO Yamauchi Materials Space-Tectonics Project (JPMJER2003). J.F.S.F. and D.G. are grateful to the Australian Research Council (ARC) Laureate Project FL160100089 for funding.

Conflicts of interests

There is no conflict to declare.

References

1 W. Ai, Z. Luo, J. Jiang, J. Zhu, Z. Du, Z. Fan, L. Xie, H. Zhang, W. Huang, T. Yu, Adv. Mater. 2014, 26, 6186-6192.
2 J. Hou, C. Cao, F. Idrees, X. Ma, ACS nano 2015, 9, 2556-2564.
3 Z. Xie, Z. He, X. Feng, W. Xu, X. Cui, J. Zhang, C. Yan, M. A. Carreon, Z. Liu, Y. Wang, ACS Appl. Mater. Interfaces 2016, 8, 10324-10333.
4 G. Tan, W. Bao, Y. Yuan, Z. Liu, R. Shahbazian-Yassar, F. Wu, K. Amine, J. Wang, J. Lu, J. Mater. Chem. A 2017, 5, 5532-5540.
5 B. J. Landi, M. J. Ganter, C. D. Cress, R. A. DiLeo, R. P. Raffaelle, Energy Environ. Sci. 2009, 2, 638-654.
6 H. Zhou, S. Zhu, M. Hibino, I. Honma, M. Ichihara, Adv. Mater. 2003, 15, 2107-2111.
7 R. Raccichini, A. Varzi, D. Wei, S. Passerini, Adv. Mater. 2017, 29, 1603421.
8 8. K. Yan, Z. Lu, H.-W. Lee, F. Xiong, P.-C. Hsu, Y. Li, J. Zhao, S. Chu, Y. Cui, Nat. Energy 2016, 1, 1-8.
9 F. D. Han, Y. J. Bai, R. Liu, B. Yao, Y. X. Qi, N. Lun, J. X. Zhang, Adv. Energy Mater. 2011, 1, 798-801.
10 Z. Jiang, Z.-J. Jiang, X. Tian, L. Luo, Electrochim. Acta 2014, 146, 455-463.
11 K. Zhang, X. Li, J. Liang, Y. Zhu, L. Hu, Q. Cheng, C. Guo, N. Lin, Y. Qian, Electrochim. Acta 2015, 155, 174-182.
12 D. W. Wang, F. Li, M. Liu, G. Q. Lu, H. M. Cheng, Angew. Chem., Int. Ed. 2008, 47, 373-376.
13 Y. Yang, S. Jin, Z. Zhang, Z. Du, H. Liu, J. Yang, H. Xu, H. Ji, ACS Appl. Mater. Interfaces 2017, 9, 14180-14186.
14 M. Lu, W. Yu, J. Shi, W. Liu, S. Chen, X. Wang, H. Wang, Electrochim. Acta 2017, 251, 396-406.
15 C. Xu, B. Xu, Y. Gu, Z. Xiong, J. Sun, X. Zhao, Energy Environ. Sci. 2013, 6, 1388-1414.
16 H. Sun, L. Mei, J. Liang, Z. Zhao, C. Lee, H. Fei, M. Ding, J. Lau, M. Li, C. Wang, Science 2017, 356, 599-604.
17 M.-H. Sun, S.-Z. Huang, L.-H. Chen, Y. Li, X.-Y. Yang, Z.-Y. Yuan, B.-L. Su, Chem. Soc. Rev. 2016, 45, 3479-3563.
18 P. Lian, X. Zhu, S. Liang, Z. Li, W. Yang, H. Wang, Electrochim. Acta 2010, 55, 3909-3914.
19 D. Pan, S. Wang, B. Zhao, M. Wu, H. Zhang, Y. Wang, Z. Jiao, Chem. Mater. 2009, 21, 3136-3142.
20 X. Hu, G. Zeng, J. Chen, C. Lu, Z. Wen, J. Mater. Chem. A 2017, 5, 4535-4542.
21 C. X. Guo, C. M. Li, Energy Environ. Sci. 2011, 4, 4504-4507.
22 G. Zhou, Y. Zhao, A. Manthiram, Adv. Energy Mater. 2015, 5, 1402263.
23 Z.Lei, N. Christov, X. Zhao, Energy Environ. Sci. 2011, 4, 1866-1873.
24 B. Ding, Z. Fan, Q. Lin, J. Wang, Z. Chang, T. Li, J. Henzie, J. Kim, H. Dou, X. Zhang, Small Methods 2019, 3, 1900277.
25 W. Li, M. Li, M. Wang, L. Zeng, Y. Yu, Nano Energy 2015, 13, 693-701.
26 C. Kim, K. S. Yang, M. Kojima, K. Yoshida, Y. J. Kim, Y. A. Kim, M. Endo, Adv. Funct. Mater. 2006, 16, 2393-2397.
27 C. Young, R. R. Salunkhe, J. Tang, C.-C. Hu, M. Shahabuddin, E. Yanmaz, M. S. A. Hossain, J. H. Kim, Y. Yamauchi, Phys. Chem. Chem. Phys. 2016, 18, 29308-29315.
28 F. Zheng, Y. Yang, Q. Chen, Nat. Commun. 2014, 5, 1-10.
29 S. W. Lee, N. Yabuuchi, B. M. Gallant, S. Chen, B.-S. Kim, P. T. Hammond, Y. Shao-Horn, Nat. Nanotechnol. 2010, 5, 531-537.
30 B. Guo, X. Wang, P. F. Fulvio, M. Chi, S. M. Mahurin, X. G. Sun, S. Dai, Adv. Mater. 2011, 23, 4661-4666.
31 S. Huang, J. Wang, Z. Pan, J. Zhu, P. K. Shen, J. Mater. Chem. A 2017, 5, 7595-7602.
32 D. Aurbach, B. Markovsky, A. Shechter, Y. Ein-Eli, J. Electrochem. Soc. 1996, 143, 3809-3920.
33 H. Cheng, J. G. Shapter, Y. Li, G. Gao, J. Energy Chem. 2021, 57, 451-468.
34 S. Yang, X. Feng, L. Zhi, Q. Cao, J. Maier, K. Müllen, Adv. Mater. 2010, 22, 838-842.
35 H. Lyu, J. Liu, S. Qiu, Y. Cao, C. Hu, S. Guo, Z. Guo, J. Mater. Chem. A 2016, 4, 9881-9889.
36 E. Yoo, J. Kim, E. Hosono, H.-S. Zhou, T. Kudo, I. Honma, Nano Lett. 2008, 8, 2277-2282.
37 H. Sun, G. Xin, T. Hu, M. Yu, D. Shao, X. Sun, J. Lian, Nat. Commun. 2014, 5, 1-8.

38 V. R. Rikka, S. R. Sahu, A. Chatterjee, P. V. Satyam, R. Prakash, M. S. Ramachandra Rao, R. Gopalan, G. Sundararajan, J. Phys. Chem. C 2018, 122, 28717−28726.